Arranz, G., Gonzalo, A., Uhlmann, M., Flores, Ó., García-Villalba, M. (2018) A Numerical Study of the Flow Around a Model Winged Seed in Auto-Rotation. *Flow, Turbulence and Combustion*, 101, pp. 477–497.

DOI: https://doi.org/10.1007/s10494-018-9945-z

Noname manuscript No.
(will be inserted by the editor)

A numerical study of the flow around a model winged seed in auto-rotation

Gonzalo Arranz[1] · **Alejandro Gonzalo**[1] · **Markus Uhlmann**[2] · **Oscar Flores**[1] · **Manuel García-Villalba**[1]

Received: date / Accepted: date

Abstract In this study the flow around a winged-seed in auto-rotation is characterized using direct numerical simulations (DNS) at Reynolds number in the range $80 - 240$, based on the descent speed and a characteristic chord length. In this range, the flow is approximately steady when observed from a reference frame fixed to the seed. For all cases, the flow structure consists of a wing tip vortex which describes a helical path, a vortex shed behind the nut of the seed and a stable leading edge vortex above the wing surface which merges with the tip vortex. With increasing Reynolds number, the leading edge vortex becomes more intense and gets closer to the wing surface. The simulation results also show the formation of a spanwise flow on the upper surface of the wing, moving fluid towards the wing tip in a region downstream and beneath the leading edge vortex. This spanwise flow is rather weak inside the core of the leading edge vortex, and the analysis of the streamlines show a very weak transport of vorticity along the vortex for the cases under consideration. The analysis of the flow suggests that the stabilization of the leading edge vortex is mainly due to non-inertial accelerations, although viscous effects may contribute, specially at lower Re. Furthermore, the leading edge vortex has been characterized by analysing the flow variables averaged along cross-sections of the vortex. While some quantities, like the spanwise velocity or the pressure inside the vortex, are rather insensitive to the threshold used to define the leading edge vortex, the same is not true for the circulation of the vortex or its averaged spanwise vorticity, due to the viscous nature of the vortex. Finally, it is observed that the spanwise vorticity scales with the angular rotation of the seed for the different Re.

Keywords direct numerical simulation · auto-rotation · leading edge vortex

Gonzalo Arranz
Tel.: +34 91 624 8220
E-mail: garranz@ing.uc3m.com

[1] Universidad Carlos III de Madrid, Spain
[2] Karlsruhe Institute of Technology, Germany

1 Introduction

Geometric and inertia properties of certain bodies induce their rotation when falling through an ambient fluid at rest. Winged seeds, or samaras, are a clear example: when they fall from their tree, they start auto-rotating thanks to their structural pattern [25]. The particular case of the samara is interesting among other auto-rotative bodies because, as it rotates, it creates a high lifting force, opposite to the gravity force, which results in a decrease of its descent speed. This "parachuting effect" increases the chance of being transported by a lateral gust wind, thus allowing the seed to spread over a wider area [11].

The auto-rotation of winged-seeds has received some attention in the literature over the last decades. Probably one of the first detailed studies on the dynamics of auto-rotation of winged-seeds is due to Norberg [25], who studied this phenomenon theoretically. Later, Azuma and Yasuda [3] report kinematic and aerodynamic parameters for different winged-seeds species, based on experimental measurements. More recent studies focus on the characterization of the parametric space where winged-seeds auto-rotate, in terms of their geometry and their mass distribution. For instance, Yasuda and Azuma [36] analyse the influence of the position of the gravity centre and the geometry of the wing, performing experiments with both real seeds and models with simplified geometries. Similarly, Varshney *et al.* [35] present a series of experiments on winged-seeds, in which sections of the wing are systematically removed until the wing surface is reduced to 30% of the original value. They report that the seed is still able to enter into auto-rotation, despite these drastic structural changes. Seter and Rosen [31] conducted a stability analysis, using a numerical model, to analyse the effect of the mass distribution of the seed on its auto-rotation. Their results show that stability is highly dependent on the chordwise distribution, being a concentrated mass towards the leading edge a necessary condition for auto-rotation. More recently, Lee and Choi [16] performed direct numerical simulations to analyse the effect of lateral wind disturbances on the trajectory of the seed. They show that in the presence of moderately strong wind (of the order of the descent velocity) the autorotation is maintained, and the seed falls at roughly the same velocity.

On the other hand, the autorotation of winged seeds has motivated the development of some bio-inspired aerial vehicles [26,9,34,29]. Lentink and co-workers found that a stable leading edge vortex (LEV), similar to the one produced in flapping wings [8], is created on the upper surface of winged seeds as they auto-rotate [19]. The presence of a stable LEV was later confirmed by Salcedo *et al.* [30] and Lee *et al.* [17] in winged-seeds of different size and shape, suggesting that leading edge vortex formation is a common mechanism in auto-rotating seeds. Due to the interest in the development of bio-inspired micro air vehicles (MAV) and the role that the LEV plays in the aerodynamic performance of flapping wings, the relevance of this discovery can be easily understood: the flow around a steadily falling seed is simpler than the fully unsteady flow over the flapping wings of animals. In the former, the LEV remains always attached, reaching a quasi-steady state. In flapping wings, a

new LEV is generated in every stroke, to be shed into the wake at the stroke reversal.

In fact, the study of LEV stability on revolving and flapping wings is a topic of active research. There is a broad literature (including both experimental and numerical studies) discussing the stabilization mechanisms of the LEV in revolving and hovering wings [10,12,15,14,18,20,5,6,28]. Although the understanding of the phenomenon is far from complete, several mechanisms have been already identified. The existence of a spanwise flow inside the LEV, which drains vorticity towards the tip, is widely accepted as a stabilization mechanism for revolving wings at $Re \gtrsim 1000$ [4,6,15]. At lower Re, the spanwise flow is weaker; thus, although vorticity transport could still balance production at the leading edge (see [28]), other mechanisms may play an important role, such as a centrifugal pumping [18], or viscous effects [14].

It is also interesting to note that, in the references of the previous paragraph, the simulations and the experiments are conducted on wings which are impulsively started and they revolve with a certain amplitude while the LEV develops. This angular amplitude is always restricted to be less than 360° to avoid the wing encountering its own wake. In the case of the winged-seed falling in ambient fluid, the seed never encounters its own wake. This, together with the low Reynolds number under consideration, means that the LEV remains always attached and steady.

Besides its advantages for the study of the dynamics of the LEV, the study of samara's auto-rotation entails several challenges. Auto-rotation is the result of the coupling between inertia and aerodynamic force, thus it is inherently a non-linear phenomenon [21]. As a consequence, the motion and attitude of the seed are not known *a priori* so that it is necessary to solve the Newton-Euler equations of the seed coupled with the Navier-Stokes equations, which provide the aerodynamic force. Therefore, the resulting motion will largely depend on the seed's shape, its mass distribution, and the fluid properties, leading to a large parametric space.

The purpose of the present paper is to characterize the flow and the LEV around a model winged-seed (with fixed shape and inertia properties) in auto-rotation, varying the Reynolds number ($Re = w_d c/\nu$, where w_d is the descent speed, c is the characteristic chord of the seed, and ν is the kinematic viscosity of the fluid). To that end, direct numerical simulations of a falling winged seed in auto-rotation are performed at Re ranging from 80 to 240. Note that, by fixing the geometry and the inertia of the seed while changing Re, it is possible to isolate its effect on the auto-rotation of the seed, both in terms of the dynamics (which will vary due to the aforementioned coupling) and in terms of the flow around the seed. The present paper focus on the analysis of the latter. Although we also briefly discuss the motion of the winged seed (since it affects the flow), the detailed analysis of the kinematics and dynamics of the seed is reported elsewhere [2].

The paper is structured as follows: Sect. 2 details the numerical model used to perform the simulations, as well as the seed model and the set-up of the

simulations; the analysis of the flow is presented in Sect. 3; and finally, several conclusions are drawn in Sect. 4.

2 Methodology

2.1 Numerical model

In the present study the descent of a model winged-seed at a constant speed w_d is considered. The seed is free to rotate along any direction and its gravity centre, G, can displace within the horizontal plane.

To simulate the motion of the seed, it is treated as a rigid body. Hence, we solve the equations of motion of the seed,

$$m_s \dot{\vec{v}}_G = \vec{F}_{ext}, \tag{1}$$

$$\mathsf{I}_G \dot{\vec{\Omega}} + \vec{\Omega} \times \mathsf{I}_G \vec{\Omega} = \vec{M}_G. \tag{2}$$

In these equations, a dot on a variable denotes its time derivative. In (1), m_s is the mass of the seed, $\vec{v}_G$ is the velocity of the seed's gravity centre and $\vec{F}_{ext}$ is the external force acting upon the seed (sum of aerodynamic force, gravity force and buoyant force). In (2), I_G is the inertia tensor of the seed with respect to G, $\vec{\Omega}$ is the angular velocity, and $\vec{M}_G$ are the external moments about G. Note that (2) holds when expressed in a body fixed reference frame, where I_G is time independent. Moreover, $\vec{M}_G$ is due only to aerodynamic forces, which is strictly true for a seed of uniform density.

In order to obtain the aerodynamic force acting upon the seed, the equations of motion are solved together with the incompressible Navier-Stokes equations. This is done with TUCAN, an in-house DNS code that solves the incompressible Navier-Stokes equations. TUCAN uses a fractional step method on a staggered grid. Spatial derivatives are discretized with centered, second-order finite differences, and a semi-implicit low-storage three-stage Runge-Kutta method is used for time integration. The presence of the body is modelled using the immersed boundary method (IBM) proposed by Uhlmann [33]. More details on the flow solver can be found in Moriche [22], which has been validated with a collection of 2D (Poiseuille flow, Taylor-Green vortices, stationary and moving cylinders and heaving and pitching airfoils [24]), and 3D flows (fully-developed turbulent channel flow, laminar flow around a sphere and heaving and pitching wings [23]).

The coupling between the Navier-Stokes equations and the equations of motion also follows the algorithm proposed by Uhlmann [33]. The coupling between the rigid-body equations for the seed and the fluid equations is weak: at each Runge-Kutta stage the aerodynamic force on the seed is computed from the flow solver, then this force is used in the rigid-body equations to update the state of the seed. The most important difference between the present code and the algorithm proposed by Uhlmann [33] is that the latter is designed to deal with spheres, where only their angular velocity and acceleration

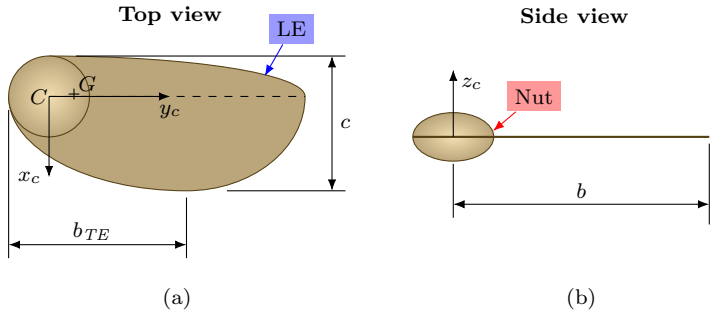

Fig. 1: Sketch of the modelled seed used in the simulations. (a) Top view, and (b) side view. Besides the characteristic dimensions of the seed, the body fixed reference frame, Σ_c (x_c, y_c, z_c), the geometric centre of the nut, C, the gravity centre, G, and the position of the leading edge (LE) are shown.

is needed (i.e., not their angular orientation). In the present simulations it is necessary to track the orientation of the seed, which is accomplished with the quaternion formulation described in Arranz *et al.* [2]. The present algorithm has been validated by computing the motion of an oblate spheroid of aspect ratio 1.5 and density ratio $\rho_s/\rho_f = 2.14$ (where ρ_s and ρ_f are the spheroid and fluid density, respectively) settling under gravity in ambient fluid, a configuration for which high-fidelity data from a boundary-conforming spectral-element method is available [7]. Using a grid resolution of 24 points per major axis, we have reproduced the instability regimes described in [7], and their transitions with increasing the Galileo number, $Ga = \sqrt{(\rho_s/\rho_f - 1)gV}/\nu$, where g is the gravity acceleration and V is the volume of the spheroid. In particular our validation runs show a steady vertical trajectory for $Ga = 96$, steady oblique for $Ga = 110$, oscillating oblique for $Ga = 122$ and vertical with lateral oscillations for $Ga = 150$.

The model of the seed has been inspired by an actual *Tipuana Tipu* seed. A sketch of the model is shown in Fig. 1. It consists of a nut, modelled as an oblate spheroid, and a flat wing, modelled with quarters of ellipses, which are tangent to each other, as proposed by Pedersen and Żbikowski [27]. We define the characteristic chord of the seed to be equal to the maximum chord, denoted c. Thus, the dimensions of the wing are given by $b = 1.9c$ and $b_{TE} = 1.32c$. The semi-major axis of the nut is $0.3c$ and the semi-minor axis is $0.18c$. Fig. 1 depicts also the body fixed reference frame Σ_c, whose origin is located at the geometric centre of the nut (point C). The axes of Σ_c are defined such that z_c is perpendicular to the wing's surface, y_c is the spanwise direction (pointing towards the wing tip), and x_c is the chordwise direction (fulfilling the right hand rule).

We prescribe the inertia of the seed in order to take into account the uneven mass distribution along the wing of the seed [25]. Thus, the gravity centre of the seed is at $\vec{CG} = -0.018c\vec{i}_c + 0.185c\vec{j}_c$ (where $\vec{CG}$ is the vector from C to

G and $\vec{i}_c$ and $\vec{j}_c$ are the unitary vectors of x_c and y_c, respectively); and the inertia tensor of the seed about C expressed in Σ_c is:

$$\mathsf{I}_C = \begin{bmatrix} 19.26 & -0.99 & 0 \\ -0.99 & 3.20 & 0 \\ 0 & 0 & 21.57 \end{bmatrix} \cdot 10^{-3} \rho_s c^5,$$

where ρ_s is the density of the seed. A more complete description of the geometric and inertial model of the seed can be found in Arranz *et al.* [2].

2.2 Computational set-up

The fluid domain employed for the simulations is a cube of length $L = 10.66c$ in which the seed is placed. Periodic boundary conditions are imposed at the lateral walls, a uniform inflow of velocity w_d is imposed at the bottom wall, and an advective boundary condition is imposed at the top boundary. The value of L has been selected after performing several simulations to ensure that the dynamics of the seed is not affected by the horizontal size of the computational domain. The grid resolution consists of 512^3 grid points, which is equivalent to 48 points per chord length. The resolution was selected after performing a grid refinement study presented in Arranz *et al.* [2]. In addition to the grid for the fluid domain, a Lagrangian grid for the seed needs to be defined. In the IBM of Uhlmann [33], the area associated to each Lagrangian point has to be roughly the same as the square of the grid spacing for the fluid domain. In the present configuration, this leads to a total number of 5674 Lagrangian points. The time step, Δt, for the temporal evolution is chosen to ensure that $CFL = u_{max}\Delta t/\Delta \leq 0.2$, where u_{max} is the maximum fluid velocity in the whole domain and $\Delta = c/48$ is the grid spacing.

To perform the simulations, the vertical position of the seed's gravity centre is fixed at $3.66c$ from the bottom boundary of the domain (i.e., inflow boundary condition). This means that the seed gravity centre can move within a horizontal plane and the seed can rotate freely about any direction. Therefore, the configuration is equivalent to a seed descending at a constant speed w_d. Consequently, for a given seed geometry and inertia, the Reynolds number, Re, and the density ratio, $\varrho = \rho_s/\rho_f$ (where ρ_f is the fluid density), univocally define the problem. For the present simulations, the density ratio is set to $\varrho = 300$, a value close to the one of real seeds falling in air (according to data extracted from Azuma and Yasuda [3]).

3 Results

Although the aim of this work is to characterize the flow, we start by summarizing the resulting motion of the seed and its variation with Re. More details can be found in Arranz *et al.* [2].

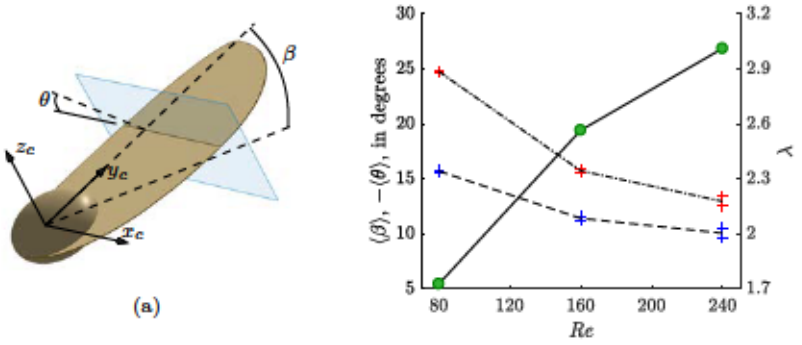

Fig. 2: (a) Definition of the seed reference frame Σ_c, and the coning (β) and pitch (θ) angles. (b) Evolution of the angles β (- - -), and θ (——), and the tip speed ratio, λ, (—●—) as a function of the Reynolds number.

For all Reynolds number investigated in this study, the seed auto-rotates at an approximately constant angular velocity about an approximately vertical axis (except for small deviations which never exceed 2° with respect to the vertical). It is interesting to recall that the problem presents hysteresis: the seed auto-rotates at $Re = 80$ if the simulation is started from a flow field obtained from a higher Re calculation, whereas it fails to auto-rotate if the simulation is initialized with a uniform flow field and an impulsive rotation of the seed. Decreasing further Re, the wing of the seed aligns with the free stream and auto-rotation stops, even for the simulations started from initial flow fields obtained from higher Re calculations.

The angular velocity and the attitude of the seed change with Re. The latter is defined by two angles: the coning angle, β, and the pitch angle, θ. The coning angle is the angle between the spanwise axis, y_c, and its projection onto the horizontal plane. The pitch angle is a geometric angle of attack: it is the angle between the chordwise axis, x_c, and the horizontal line contained in a plane perpendicular to y_c. Both angles are depicted in Fig. 2a.

Fig. 2b shows the variation with Re of β, θ and the tip speed ratio, defined as $\lambda = \Omega b/w_d$, being Ω the average angular velocity. It should be noted that the motion of the seed is such that both the coning angle and the pitch angle present small oscillations about a mean value. Therefore, Fig. 2b shows the mean value of β and θ, together with their standard deviation, depicted as vertical bars. From Fig. 2b it is observed that while λ increases with Re (i.e., the seed spins faster with Re), both the coning angle and the pitch angle decrease in magnitude. This means that, with increasing Re, the seed's wing becomes more aligned with the horizontal plane.

The changes in the kinematics of the seed have an impact on the flow around the seed. This is illustrated in Fig. 3, that displays iso-surfaces of the

(a) (b) (c)

Fig. 3: Iso-surfaces of the second invariant of the velocity gradient tensor, Q, for (a) $Re = 80$, (b) $Re = 160$, and (c) $Re = 240$. Light grey surface corresponds to $Q = 0.75\Omega^2$ and dark grey surface corresponds to $Q = 12\Omega^2$ for each case.

second invariant of the velocity-gradient tensor, Q [13], for $Re = 80$, $Re = 160$ and $Re = 240$. Since the angular velocity changes with Re and the descent velocity is constant for all the cases, we choose Ω^2 to non-dimensionalize Q in order to facilitate the comparison between the various cases. Three main vortical structures can be identified for all Re: a wing tip vortex, a vortex shed behind the nut, and an LEV which is formed above the wing and corresponds to the darker grey surface in Fig. 3. The wing tip vortex wraps around a vertical axis yielding a helical structure, whose pitch decreases with increasing Re, indicating a faster rotation. The vortex shed behind the nut also forms an helix with the same sense of rotation but smaller radius than the wing tip vortex. This suggests that the axis of rotation is close to the nut (indeed it is found approximately at the gravity centre [2]). Finally, the LEV seems to become more intense with increasing Re, especially when comparing the cases $Re = 80$ and 160. Note that the intensity of the LEV is usually related to the lift, so that a more intense LEV results in a larger lift on the wing [2].

As discussed above, the coning angle, β, the pitch angle, θ, and the angular velocity remain approximately constant as the seed falls, for a given Reynolds number. As a consequence, and due to the low Reynolds number, the flow around the seed is approximately steady when observed from a reference frame fixed to the seed. Therefore, it seems appropriate to study the flow variables with respect to the seed's reference frame Σ_c. Thus, the time-averaged relative velocity of a given point, $\vec{x}$, is

$$\vec{u}(\vec{x}) = \frac{1}{T}\int_0^T \left(\vec{U} - \vec{v}_G - \vec{\Omega} \times \vec{r}\right) dt, \tag{3}$$

where $\vec{U}$ is the instantaneous absolute velocity, $\vec{v}_G$ is the velocity of the seed's gravity centre, $\vec{\Omega}$ is the instantaneous angular velocity and $\vec{r}$ is the vector position from G to $\vec{x}$. Note that all the vectors in (3) need to be expressed in Σ_c. For the present cases, the time average is performed over the last 2 revolutions run in the simulation, discarding an initial transient whose duration varies with the Reynolds number from about 10 revolutions for $Re = 80$ to 30 revolutions for $Re = 240$ (see Arranz *et al.* [2]). Thus, $T \approx 4\pi/\Omega$, where Ω is the averaged angular velocity of the seed. Similarly, the time-averaged relative vorticity is defined as $\vec{\omega} = \nabla \times \vec{u}$, where again the curl is taken in the seed's reference frame Σ_c. From now on, all relative flow variables are implicitly assumed to be averaged in time.

The second invariant of the time-averaged relative-velocity-gradient tensor, q, can also be expressed in terms of the time averaged value of Q, the mean angular velocity, $\Omega\,\vec{k}$ (being $\vec{k}$ the unit vector parallel to the rotation axis), and $\vec{\omega}$,

$$q = \frac{1}{T}\int_0^T Q dt - \Omega^2 - \Omega\,\vec{k}\cdot\vec{\omega}. \tag{4}$$

Surfaces of constant q will be used in the following sections to identify and characterize the LEV. Relevant quantities like the circulation of the LEV will be shown to depend on the particular threshold value of q chosen to identify the vortex, henceforth denoted as q_{th}. Note that the range of q_{th} to be employed is implicitly limited by (4). At the inflow, Q and the absolute vorticity are zero, so that $\vec{\omega} = -2\Omega\,\vec{k}$ and $q = \Omega^2$. Therefore, the threshold, q_{th}, to be used to identify the LEV has to be several times larger than q at the inflow.

3.1 Flow characterization

The flow around the winged seed, even when observed from Σ_c, is 3D and rather complex, as it can be appreciated in Fig. 3. Hence, in order to characterize the flow, we analyze it first in spanwise cross-sections. Three planes are selected, namely $y_c = 0.25b$, $y_c = 0.5b$ and $y_c = 0.75b$, as sketched on top of Figs. 4-6.

First, we analyze the relative spanwise vorticity in Fig. 4 since this is the main component of the vorticity in the LEV. In the figure, contours of ω_y, are shown for the three cases, at the three spanwise locations mentioned above. In addition to the vorticity contours, contours of q for the thresholds $6\Omega^2$ and $12\Omega^2$ are also displayed in the figure. This gives an indication of the position of the LEV along the span for the different Re. Note that the contours are normalized with the maximum spanwise vorticity (computed in the fluid domain defined by $y_c = [0.3c, 1.9c]$ and the limits shown in Fig. 4), $\omega_{y,\max} c/w_d = [46, 85, 107]$, for $Re = 80, 160$ and 240, respectively. Therefore, it should be borne in mind that the intensity of the vorticity field shown in Fig. 4 increases with the Reynolds number. For all spanwise positions, the contours of ω_y and the contours of q look qualitatively similar, and, as expected, the maximum of ω_y is found inside the LEV. The main difference between the

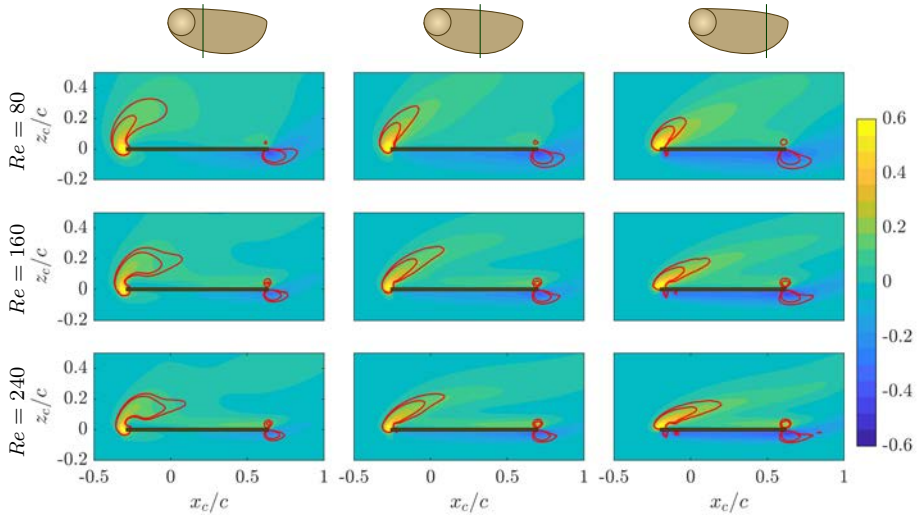

Fig. 4: Contours of the spanwise vorticity, ω_y, normalized with the maximum spanwise vorticity for each Re. Each row corresponds to a different Reynolds number. The columns correspond (from left to right) to spanwise positions at 25%, 50% and 75% of the span. For a visualization, the corresponding spanwise plane is sketched above the column. Red contours correspond to the intersection of the iso-surfaces of $q = 6\Omega^2$ and $q = 12\Omega^2$ with the plane.

three cases is that with increasing Re the LEV gets closer to the wing surface, all along the span.

In the literature, the presence of an LEV near the wing surface is associated with lift augmentation as a result of the low-pressure region developed in the core of the LEV [19]. Fig. 5 shows the contours of the pressure (relative to the pressure at the inflow) normalized with the absolute value of the minimum pressure for each Reynolds number, $p_{\min}/(\rho_f w_d^2) = [1.3, 2.4, 3.0]$ for $Re = 80$, 160 and 240, respectively. Regardless of Re and the spanwise section, there is a low pressure region above the wing whose peak is located near the LEV. This low pressure region seems to be narrower near the wing root (see left panels of Fig. 5, $y_c = 0.25b$) and it widens towards the wing tip (see right panels of Fig. 5, $y_c = 0.75b$). Note that, as a result of larger pressure difference with Re (recall that the values are normalized with $p_{\min}$, which is larger for higher Re), larger lifting forces are developed for the higher Reynolds numbers [2].

As discussed in the introduction, the stability of the LEV in revolving wings has been widely studied in the literature. Several authors suggest that the stabilization may be linked to the development of a spanwise flow over the wing surface [4,6,28,19]. Therefore, it is interesting to analyze the relative spanwise velocity, u_y, for the present cases. This velocity is shown in Fig. 6 at the same spanwise locations studied above. As before, u_y is normalized with

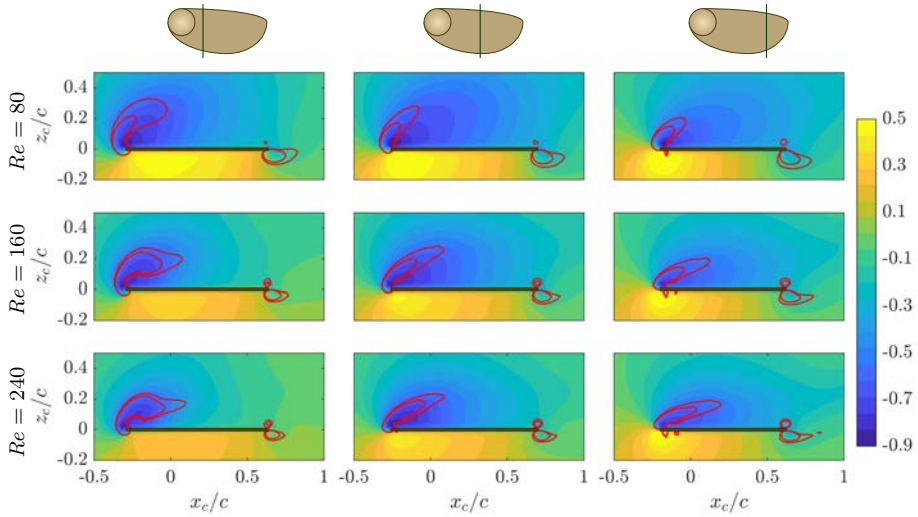

Fig. 5: Contours of the pressure normalized with the absolute value of the minimum pressure for each Re. Each row correspond to a different Reynolds number. The columns correspond (from left to right) to spanwise positions at 25%, 50% and 75% of the span. For a visualization, the corresponding spanwise plane is sketched above the column. Red contours correspond to the intersection of the iso-surfaces of $q = 6\Omega^2$ and $q = 12\Omega^2$ with the plane.

the maximum spanwise velocity for each Re, $u_{y,\max}/w_d = [0.89, 1.10, 1.44]$. First of all, a chordwise gradient of u_y is observed for all cases. This velocity gradient, which yields a positive u_y upstream and a negative u_y downstream is due to the wing rotation, i.e. the last term of (3). Besides this linear variation, a region of positive spanwise velocity is found above the wing, for all cases. This spanwise flow (except near the nut) is behind and below the LEV, and the peak of maximum u_y never coincides with the core of the LEV but it is downstream and beneath it. Its intensity decreases towards the tip and with decreasing Re. Particularly, it is barely appreciable for $Re = 80$, whereas it reaches a maximum at $y_c = 0.25b$ for $Re = 240$ (left panel of Fig. 6), being approximately equal to 40% of the tip velocity.

The increase of the intensity of this spanwise flow with Re may be linked to the centrifugal and Coriolis accelerations, as reported in previous works [32, 1]. Fig. 7 displays the contribution of these terms to the spanwise momentum equation (namely, $-[\vec{\Omega} \times \vec{\Omega} \times \vec{r} + 2\vec{\Omega} \times \vec{u}] \cdot \vec{j}_c$), normalized with its maximum value for each Re, namely, $1.76w_d^2/c$, $4.53w_d^2/c$ and $6.51w_d^2/c$ for $Re = 80$, 160 and 240, respectively. These fictitious accelerations are positive in the region where the spanwise flow is present, and they increase with Re, in agreement with the spanwise flow behind the LEV shown in Fig. 6.

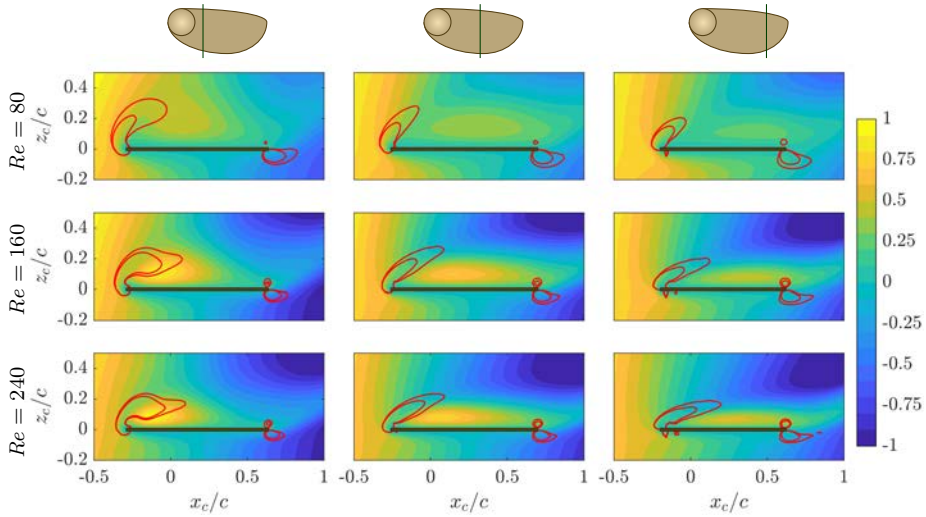

Fig. 6: Contours of the spanwise velocity, u_y, normalized with the maximum spanwise velocity for each Re. Each row correspond to a different Reynolds number. The columns correspond (from left to right) to spanwise positions at 25%, 50% and 75% of the span. For a visualization, the corresponding spanwise plane is sketched above the column. Red contours correspond to the intersection of the iso-surfaces of $q = 6\Omega^2$ and $q = 12\Omega^2$ with the plane.

The spanwise velocity and vorticity contours shown in Fig. 4 and 6 are qualitatively similar to those observed in the flow around revolving and flapping wings at similar Re [5,6,28,18,12]. It should be noted that, in these references the Reynolds number is expressed in terms of the mean chord and the velocity of the wing tip, which yields Reynolds numbers equal to $[121, 337, 584]$ in the present case.

3.2 Spanwise flow and stabilization of the LEV

The fact that the maximum u_y in Fig. 6 does not occur inside the LEV seems to suggest that, at least for the geometry, kinematics and Reynolds numbers considered here, the stability of the LEV (i.e., the fact that it is not shed into the wake) is not linked to a spanwise flow inside the vortex. Recall that, as mentioned in the introduction, several authors argue that the vorticity transport along the LEV produced by the spanwise flow contributes to the stability of the LEV for $Re \gtrsim 1000$ [4,6,28]. However, while Fig. 6 shows that the maximum of u_y is registered outside of the LEV, it does not show whether the weaker u_y inside the LEV is strong enough to produce vorticity transport along the LEV. To test this hypothesis, we compute the streamlines of the relative velocity field. Note that, since the flow is steady with respect to Σ_c,

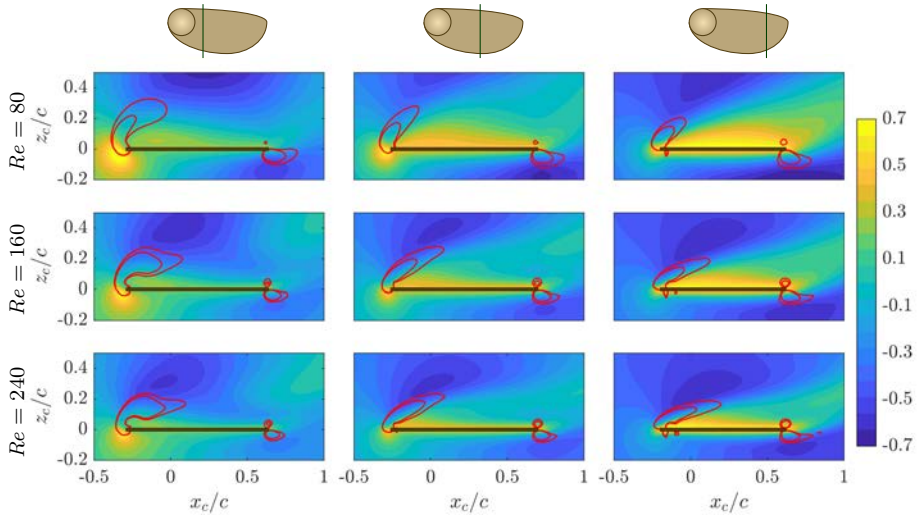

Fig. 7: Contours of the spanwise component of the centrifugal and Coriolis accelerations normalized with its maximum for each Re. Each row correspond to a different Reynolds number. The columns correspond (from left to right) to spanwise positions at 25%, 50% and 75% of the span. For a visualization, the corresponding spanwise plane is sketched above the column. Red contours correspond to the intersection of the iso-surfaces of $q = 6\Omega^2$ and $q = 12\Omega^2$ with the plane.

the streamlines of the relative velocity correspond to the path lines followed by the fluid particles as they move past the rotating seed. These streamlines are shown in Fig. 8, for the three Re under study.

Particularly, Fig. 8 shows the streamlines crossing the plane $y_c = 0.5b$ above the wing surface at prescribed seeding points uniformly spaced in the plane. Streamlines crossing the plane $y_c = 0.5b$ inside the LEV (defined as the iso-surface of $q_{th} = 6\Omega^2$) are colored with the velocity magnitude, while streamlines crossing $y_c = 0.5b$ between the LEV and the wing surface are colored in blue. The rationale between this differentiation is to compare the behaviour of the fluid particles inside the LEV to those moving outward through the region of maximum u_y.

Fig. 8 shows that the fluid particles that enter the LEV come from the pressure side (lower surface of the wing): they are accelerated as they turn around the leading edge of the seed, and they leave the LEV without travelling inside it along its longitudinal axis. On the contrary, fluid particles beneath the leading edge vortex do not seem to come from the leading edge but from the vortex at the nut, and they travel longer distances along the wing span before leaving the wing. The same behaviour is observed for the streamlines in the three Reynolds numbers under study, although the spanwise distance

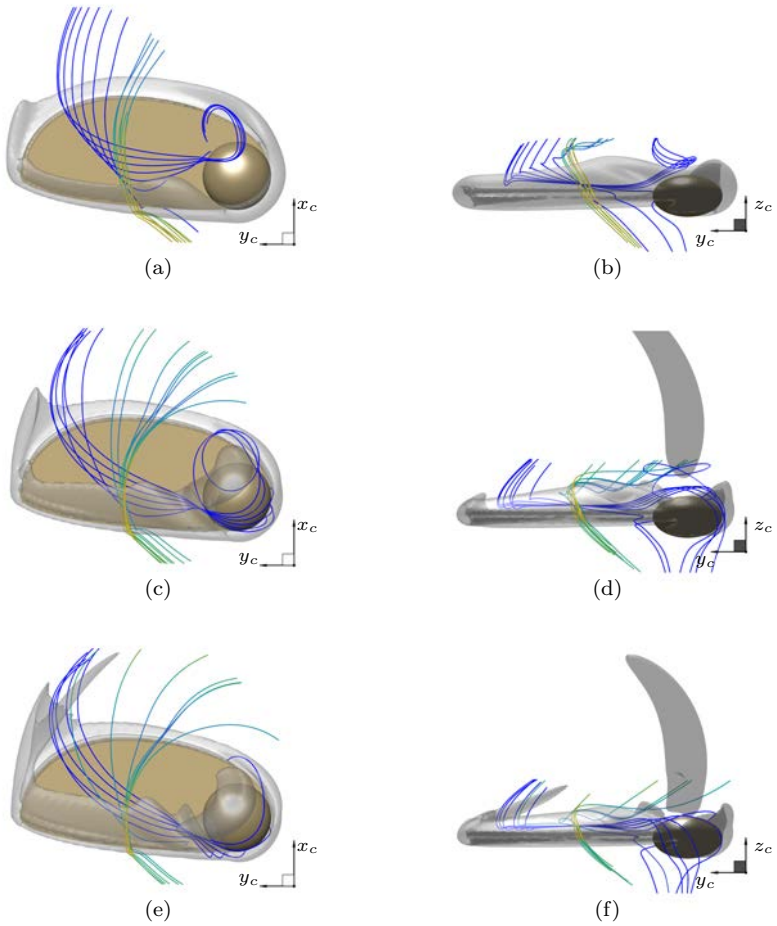

Fig. 8: Streamlines at plane $y_c = 0.5b$. Streamlines whose intersection with $y_c = 0.5b$ lies inside the LEV (for $q = 6\Omega^2$, also shown) are colored by its velocity intensity. Blue streamlines beneath and downstream the LEV. (a) Top view and (b) side view for $Re = 80$. (c) Top view and (d) side view for $Re = 160$. (e) Top view and (f) side view for $Re = 240$.

travelled by the streamlines beneath the LEV (blue lines in Fig. 8) becomes larger as Re increases, as it may be expected from the larger spanwise velocity observed in Fig. 6.

Note that the same behaviour is observed for streamlines defined at different y_c planes, and for different q_{th} in the definition of the LEV. To demonstrate this, we compute streamlines passing through seeding points uniformly distributed in the volume of the LEV, defined as the region with $q \geq 6\Omega^2$. We compute approximately 4.5×10^4 streamlines for each Re, storing the y_c co-

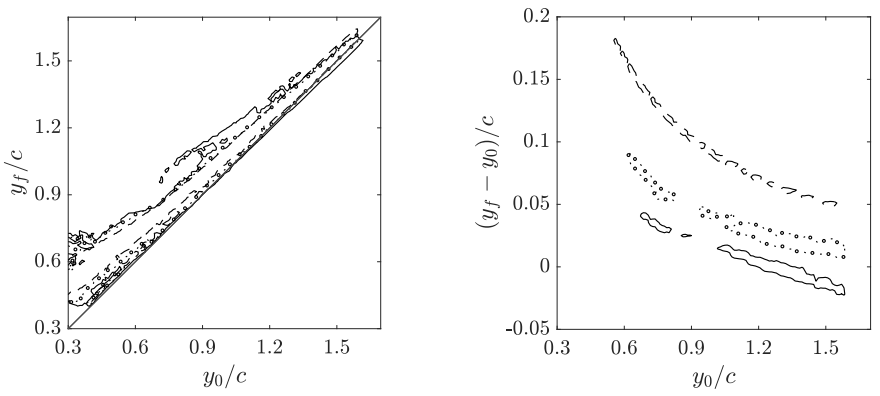

(a) (b)

Fig. 9: (a) JPDF of y_0 and y_f. The iso-contour contains 95% of the JPDF. (b) JPDF of y_0 and the spanwise travelled distance $y_f - y_0$. The iso-contour contains 20% of the JPDF, which provides an approximation to the mode of the JPDF. Note the different scale of the abscissa and the ordinate in (b). In both panels, line styles correspond to a different Re: (- - -) $Re = 80$, (-∘-) $Re = 160$ and, (——) $Re = 240$.

ordinate of the point where each streamline enters and exits the LEV, y_0 and y_f, respectively. These data is used to compute the joint probability density functions (JPDFs) shown in Fig. 9.

Fig. 9a shows an iso-contour containing 95% of the JPDF of y_0 and y_f. It can be observed that the JPDF is very similar for all Re. It mostly lies on the region $y_f > y_0$, corresponding to fluid particles travelling along the wing span inside the LEV towards the wing tip. For $y_0/c \lesssim 0.6$ the effect of increasing the Re is to have shorter displacements along the wing span (i.e., the contour gets closer to the line $y_0 = y_f$). A similar behaviour is observed near the wing tip, where the JPDF of case $Re = 240$ shows values $y_f < y_0$ (i.e., fluid particles travelling inward). This is better observed in Fig. 9b, where an iso-contour of the JPDF of $y_f - y_0$ and y_0 is shown (containing 20% of the JPDF). Note that this iso-contour roughly shows the mode of the JPDF (i.e. the most probable values of the JPDF at each y_0). The spanwise distance travelled by the fluid particles inside the LEV decreases as Re increases for all spanwise sections, in agreement with the visualizations in Fig. 8. Also, as streamlines closer to the wing tip are considered, the travelled distance $(y_f - y_0)$ becomes smaller, changing sign for $Re = 240$ for $y_0/c \approx 1.2 - 1.3$. This decrease of the travelled distance may be a combination of two factors. On the one hand, as it can be inferred from Fig. 6, the spanwise velocity in the LEV decreases from the nut to the wing tip. On the other hand, the chordwise velocity increases with y_0 (being roughly proportional to $\Omega y_0 \cos\beta$), and with Re (due to the larger rotational velocity and the decrease in the coning angle). The change of sign

(i.e., change of direction) of the travelled distance is probably due to the wing tip vortex, i.e. an effect of the flow around the tip from the lower surface to the upper surface of the wing. This effect becomes more noticeable for larger Re, since β decreases. Moreover, Fig. 9b shows that for $y_0 > c$ the difference in $(y_f - y_0)$ for the different Reynolds number becomes of the same order as the change of $w_d \sin\beta$ with Re. This fact might suggest that the spanwise flow inside the LEV is mainly due to β (i.e., the projection of the descent speed along the spanwise direction), rather than to rotational accelerations. This is supported by Fig. 7, where it is observed that the magnitude of these accelerations is small inside the LEV.

Overall, the analysis of the streamlines shows a spanwise flow inside the LEV that becomes less dominant as Re increases. On the other hand, the spanwise flow increases with Re outside of the LEV, as it has been discussed in Fig. 6. From this point of view, our results do not seem to be consistent with a scenario where the LEV is stabilized by vorticity transport within the LEV itself.

At the present range of Reynolds number, LEV stability could be due to viscous effects. For a sufficiently low Re, Jardin [14] argues that the stability of the LEV at a given spanwise section is solely determined by its local Re and its effective angle of attack, as in a 2D wing. Hence, in order to evaluate the stabilization of the LEV due to viscous effects, we compute the local Reynolds number, Re_{y_c}, and the effective angle of attack, α, at each spanwise section. The local Reynolds number is based on the local chord, $c(y_c)$, and the local effective velocity, $\vec{u}_e(y_c)$. This velocity is the projection of the rigid body velocity along the y_c axis (dashed line in Fig. 1) onto the plane perpendicular to this axis. Mathematically, its modulus is

$$u_e(y_c) = \sqrt{(\vec{v}(y_c) \cdot \vec{i}_c)^2 + (\vec{v}(y_c) \cdot \vec{k}_c)^2}, \tag{5}$$

where $\vec{v}(y_c) = \vec{v}_G + \vec{\Omega} \times (y_c\vec{j}_c - \vec{CG})$. The modulus of the effective velocity is depicted in Fig. 10a for each Re. On the other hand, the effective angle of attack, $\alpha(y_c)$, is the angle between $\vec{u}_e(y_c)$ and the wing chordwise direction.

Fig. 10b shows, for each case, the effective Reynolds number, Re_{y_c}, as a function of the effective angle of attack. For reference, several characteristic spanwise sections have been marked. It can be observed that α is high near the nut (between $60° - 70°$) and decreases towards the tip (until $\sim 10°$). The effective Re increases towards the tip due to the higher u_e until $y_c \approx 0.75b$, dropping to zero for spanwise sections beyond 75% of the span because of the sharp decrease of $c(y_c)$ near the wing tip. The region below the dashed line in Fig. 10b would correspond to the spanwise sections whose LEV might be stabilized by viscous effects. Hence, for $Re = 160$ and 240, only for $y_c \geq 0.75b$ the LEV might be stabilized due to this phenomenon. Meanwhile for $Re = 80$, this threshold would extend up to $y_c \geq 0.5b$. Therefore, viscosity does not seem to be a plausible candidate to explain LEV stability, specially for $Re = 160$ and 240, since it would only be dominant near the tip, where the LEV has tilted and merged with the wing tip vortex.

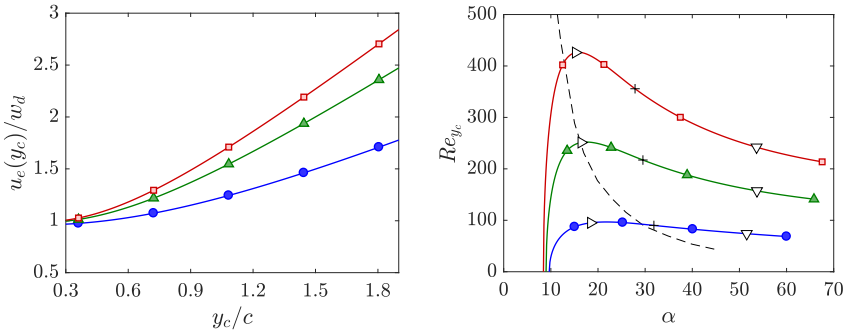

(a) (b)

Fig. 10: (a) Variation of the modulus of the effective velocity along y_c. (b) Effective Reynolds number at y_c versus the effective angle of attack at the same spanwise location. Characteristic spanwise sections are marked at 25% (▽), 50% (+), and 75% (▷) of the span. Dashed line in (b) correspond to the theoretical 2D-viscous stability limit (extracted from Zhang *et al.* [37]). In both panels, (–●–)$Re = 80$, (–▲–)$Re = 160$, and (–□–)$Re = 240$.

Having discarded vorticity transport along the spanwise direction and having analysed the importance of viscous effects, Coriolis and centrifugal effects (referred to as centrifugal pumping in the present paper) may play a role in the attachment of the LEV. The importance of non-inertial effects have been already recognised in the development of an spanwise flow behind the LEV for the present cases. According to several authors [18,12,14], fictitious forces would contribute to the attachment of the LEV for Rossby numbers, Ro, of order unity. Defining Ro as in Hargib *et al.* [12], namely $Ro = u_{tip}/\Omega b$, where $u_{tip} = \sqrt{w_d^2 + \Omega b}$, it is found that $Ro = \sqrt{\lambda^2 + 1}/\lambda$, which, in the cases presented here, ranges from 1.2 to 1. Consequently, centrifugal pumping would be a feasible candidate for the stabilization of the LEV in the cases analysed here. Nevertheless, the exact mechanisms by which fictitious forces stabilize the LEV in the present case are still not clear.

3.3 Leading edge vortex characterization

We now proceed to a more detailed characterization of the LEV. To that end we average the relative velocity ($\langle u_y \rangle$), relative vorticity ($\langle \omega_y \rangle$) and pressure ($\langle p \rangle$) inside the LEV (regions where $q > q_{th}$) in planes of constant y_c. These averages are performed for different values of q_{th}, in order to assess the dependence of the averaged values upon the particular threshold used in the identification of the LEV. Fig. 11 depicts the three variables along the LEV for each Re and for q_{th}/Ω^2 in the range $6 - 12$. They are normalized with the descent speed, w_d, the characteristic chord, c, and ρ_f.

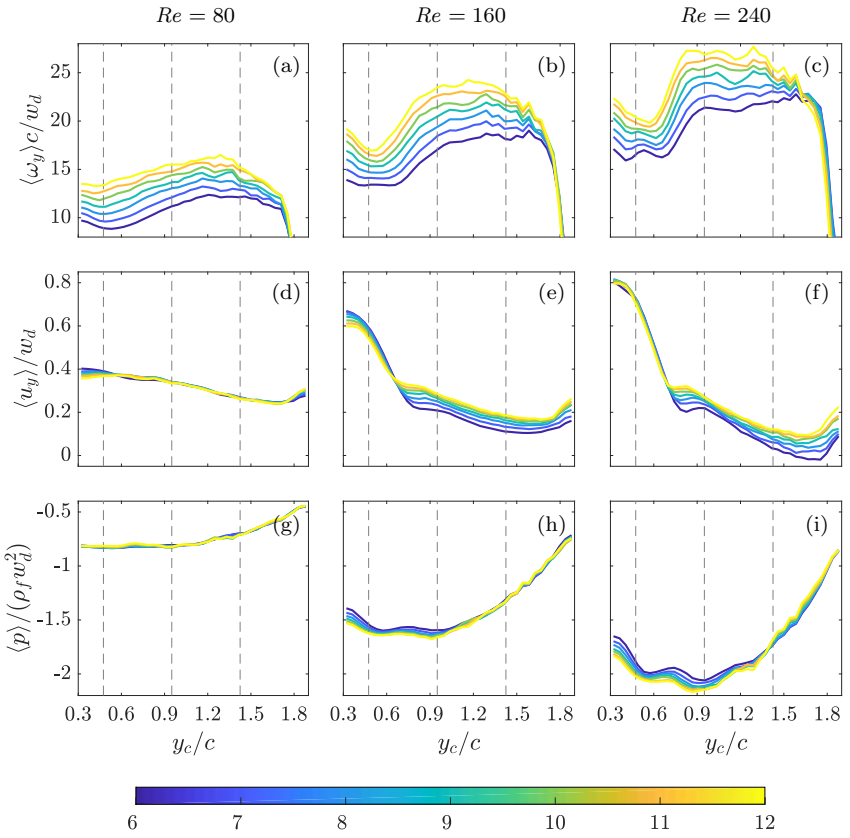

Fig. 11: Relative spanwise vorticity averaged over the LEV cross-sections, $\langle\omega_y\rangle c/w_d$, as a function of y_c for (a) $Re = 80$, (b) $Re = 160$, and (c) $Re = 240$. Relative spanwise velocity averaged over the LEV cross-sections, $\langle u_y\rangle c/w_d$, as a function of y_c for (d) $Re = 80$, (e) $Re = 160$, and (f) $Re = 240$. Pressure averaged over the LEV cross-sections, $\langle p\rangle/(\rho w_d^2)$, as a function of y_c for (g) $Re = 80$, (h) $Re = 160$, and (i) $Re = 240$. Different q_{th}/Ω^2 values have different color intensity, as shown in the colorbar. Dashed lines correspond to the 25%, 50% and 75% spanwise sections (Fig. 4-6).

Fig. 11a-c shows $\langle\omega_y\rangle$ for the different Re and q_{th}. Regardless of q_{th} and Re, $\langle\omega_y\rangle$ slightly decreases from the nut to 25% of the span, and then it increases until reaching a plateau. This increase becomes steeper as Re increases. At the wing tip, $\langle\omega_y\rangle$ abruptly decreases, due to the merging of the LEV into the wing tip vortex, with the consequent change of direction of the vorticity. At a given spanwise section and q_{th}, $\langle\omega_y\rangle$ increases with Re. On the other hand, $\langle\omega_y\rangle$ increases with q_{th} for all Re analyzed., This indicates that ω_y is not constant inside the cross sections of the LEV, as it corresponds to a viscous vortex.

The relative spanwise velocity averaged over the LEV is displayed in Fig. 11d-f. Note that, contrary to $\langle\omega_y\rangle$, $\langle u_y\rangle$ is fairly independent of q_{th} for a given Re. Therefore, we can focus the discussion on the evolution of $\langle u_y\rangle$ along the LEV and the effect of the Reynolds number. For all cases we observe that $\langle u_y\rangle$ decreases towards the tip, although the profiles for $Re = 160$ and 240 differ considerably from the profile for $Re = 80$. In particular, the negative gradient of $\langle u_y\rangle$ along the span is much less pronounced for $Re = 80$ than for the higher Re. The latter profiles present a steep gradient up to $y_c \approx 0.7$ and a milder one beyond that location. This higher spanwise velocity near the nut is due to the spanwise flow, developed presumably due to non-inertial forces, which partially coincides with the LEV for $Re = 160$ and 240 and it is not present for $Re = 80$ (see Fig. 6). Except in this region, $\langle u_y\rangle$ decreases with Re, in agreement with the behaviour of the streamlines (see discussion of Fig. 9b).

As commented before, the decrease of spanwise flow in the LEV with increasing Re seems to be related to the attitude of the seed: the coning angle is larger at lower Re, which implies a larger projection of the descent velocity w_d along the spanwise direction of the wing, y_c.

The pressure averaged over the LEV cross-sections, $\langle p\rangle$, is depicted in Fig. 11g-i for the different Re. Similarly to $\langle u_y\rangle$, the averaged pressure is also largely independent of q_{th}. Throughout the span, lower pressures are found for increasing Re, which suggests that the lift force of the winged seed increases with Re (as confirmed in Arranz *et al.* [2]). For all Re, the pressure increases towards the tip for $y_c \gtrsim 0.9c$, producing and adverse pressure gradient which becomes stronger as Re increases. Note that, while the projection of w_d along the spanwise direction of the seed could explain the intensity of $\langle u_y\rangle$, the presence of an adverse pressure gradient might explain why $\langle u_y\rangle$ decreases towards the wing tip.

Note that the variables shown in Fig. 11 are normalized with magnitudes which remain constant regardless of Re. Hence, it is interesting to use a normalization in which the effect of the Reynolds number is somehow involved. Fig. 12a-d depicts $\langle u_y\rangle$, $\langle p\rangle$ and $\langle\omega_y\rangle$ normalized with c, ρ_f and the effective velocity at y_c. Note that by employing $u_e(y_c)$ as the characteristic velocity, we are accounting for the change in the angular speed and for the change in the seed's attitude. Fig. 12 shows $\langle u_y\rangle$, $\langle p\rangle$ and $\langle\omega_y\rangle$ for $q_{th} = 9$. Additionally, the shaded regions correspond to the variation with the threshold, $q_{th} = [6 - 12]$ for each variable and Re. Fig. 12a and Fig. 12b reveal that, upon this normalization, the cases $Re = 160$ and 240 tend to collapse, contrary to the case $Re = 80$. This behaviour is also observed in the aerodynamic forces (see Arranz *et al.* [2]), and seems to suggest that auto-rotation at $Re = 80$ differs from auto-rotation at higher Re (within the range of study). Nonetheless, it has been already mentioned that the case with $Re = 80$ is somewhat anomalous since for example its auto-rotation depends on the initial conditions (hysteresis).

Regarding $\langle\omega_y\rangle$, it is interesting to recall that, although using $u_e(y_c)$ as the characteristic velocity (Fig. 12c) yields a result similar to Fig. 12a-b, using Ωc instead, results in a collapse of the profiles of $\langle\omega_y\rangle$ for all Re, except close to the nut ($y_c < 0.8c$), where the case $Re = 80$ differs from the other two cases.

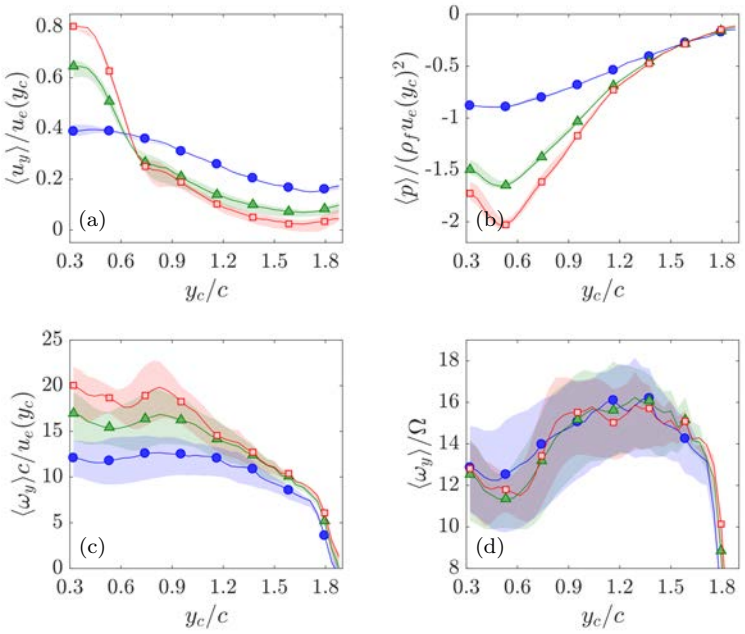

Fig. 12: (a) Relative spanwise velocity averaged over the LEV cross-sections normalized with $u_e(y_c)$. (b) Relative pressure averaged over the LEV cross-sections normalized with $\rho_f c u_e(y_c)$. (c) Relative spanwise vorticity normalized with $c/u_e(y_c)$, and (d) with Ω. (—●—)$Re = 80$, (—▲—)$Re = 160$ and (—□—)$Re = 240$. Shaded regions correspond to the variation with $q_{th} = [6 - 12]$.

This can be appreciated in Fig. 12d, and it is also true for other q_{th}. This suggests that the characteristic velocity for chordwise and vertical velocities is Ωc, even if the precise cause for this scaling is not clear at the present time.

Finally, we conclude the characterization of the LEV by computing the spanwise circulation inside the LEV, Γ, since it is usually employed to relate the intensity of the LEV to the aerodynamic force. We compute Γ as the integral of ω_y over the LEV cross-sections. This circulation is shown in Fig. 13 for different thresholds q_{th}, and for the three Reynolds numbers considered here. Note that, if ω_y were concentrated in a finite surface (i.e., a vortex tube), then Γ would become independent of q_{th} for a sufficiently low value of the threshold. However, Fig. 13 shows Γ increasing monotonously as q_{th} decreases, with no sign of a plateau. This is the expected behaviour for a viscous vortex, as it corresponds to a low-Reynolds number flow. An important consequence of the lack of collapse of Γ with q_{th} in Fig. 13 is that Γ can hardly be used to characterize the aerodynamic force on the wing at the present Re. Note that this approach is usually found in the literature for winged seeds at higher Re [19,28].

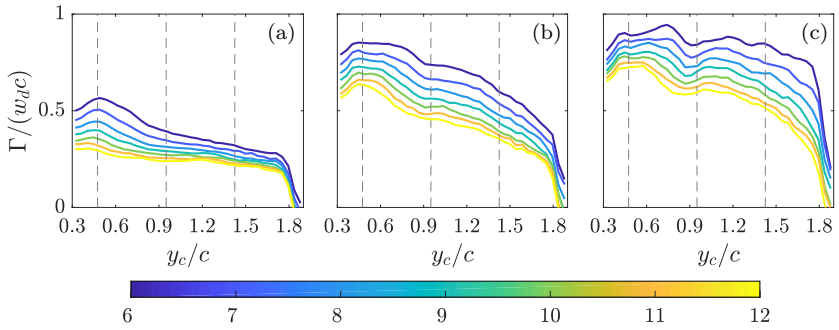

Fig. 13: Circulation averaged over the LEV cross-sections, $\Gamma/(w_d c)$, as a function of y_c. (a) $Re = 80$, (b) $Re = 160$, and (c) $Re = 240$. Different q_{th}/Ω^2 values have different color intensity, as shown in the colorbar.

4 Conclusions

Numerical simulations of the auto-rotation of a winged-seed at Re in the range $80 - 240$ have been performed. The seed, for all cases under study, reaches a state of stable auto-rotation with approximately constant angular velocity and attitude, which vary with Re. Due to this, and to the low Reynolds number, the flow is approximately steady when observed from a reference frame fixed to the seed, so that this perspective has been employed in the flow characterization. Three vortical structures are formed near the seed: a wing tip vortex which describes a helical path; a vortex shed behind the nut; and a stable LEV above the wing surface which merges with the tip vortex.

We have characterized the flow over the wing surface by analyzing the relative spanwise vorticity, the relative spanwise velocity and the pressure at various spanwise sections. With increasing Reynolds number, the flow visualizations show that the LEV becomes more intense and gets closer to the wing surface. For all cases the low pressure peak on the wing surface is located in the neighbourhood of the LEV. We have also identified the formation of a spanwise flow on the wing surface, which is more intense downstream and beneath the LEV. This flow topology is directly linked to Coriolis and centripetal accelerations and is in agreement with flows around revolving wings found in the literature.

We have explored the three possible mechanisms for the stabilization of the LEV reported in the literature, namely, the vorticity transport within the LEV, viscous effects and centrifugal pumping. The first mechanism has been evaluated via a statistical analysis of fluid particle trajectories along the LEV. We have found no evidence of significant vorticity transport along the LEV for the flow under consideration. The evaluation of the viscous stabilization of the LEV has been performed in terms of the local Re and local angle of attack of

the corresponding wing section. The results suggest that this mechanism can only be important near the tips, but the 3D character of the flow in this region makes it unlikely. Finally, the stabilization via non-inertial accelerations seems to be a potential candidate, since the Rossby number is of order unity in the present study.

To conclude, the flow inside the LEV has been characterized, studying the variation of average flow magnitudes inside the LEV with different q thresholds. The average spanwise velocity and the pressure inside the LEV do not seem to depend on the q value. We also found that $\langle u_y \rangle$ decreases for increasing Re, contrary to the behaviour of the spanwise flow outside the LEV.

The average spanwise vorticity inside the LEV, $\langle \omega_y \rangle$, for a given Re depends on the value of q. On the contrary, for a given q, $\langle \omega_y \rangle$ is quantitatively similar for the different Re when scaled with Ω, suggesting that both the chordwise and vertical velocity components scale with the angular speed. The multiplication of $\langle \omega_y \rangle$ by the cross-sectional area of the LEV to compute its spanwise circulation, Γ, yielded that it largely depends on the q value, as it should be expected for a low-Reynolds flow. Hence, the aerodynamic forces cannot be inferred from Γ, contrary to what can be done with reasonable accuracy at higher Re.

Overall, we observe that the flow around the auto-rotating seed for $Re = 160$ and 240 is qualitatively different compared to $Re = 80$. This result may be explained by the fact that $Re = 80$ seems to be close to the lower limit where auto-rotation is possible (for the seed considered here).

Compliance with Ethical Standards:

Funding: This work was supported by grants TRA2013-41103-P (Mineco/Feder UE) and DPI2016-76151-C2-2-R (AEI/ Feder UE). MGV was partially supported by a grant of the BBVA Foundation. The code was partially developed during a stay of MGV (funded by the Spanish Ministry of Education through the program José Castillejo) at the Karlsruhe Institute of Technology. The simulations were partially performed at the Steinbuch Centre for Computing (SCC), Karlsruhe.

Conflict of Interest: The authors declare that they have no conflict of interest.

References

1. Aono, H., Liang, F., Liu, H.: Near- and far-field aerodynamics in insect hovering flight: an integrated computational study. J. Exp. Biol. **211**(2), 239–257 (2008). doi:10.1242/jeb.008649
2. Arranz, G., Moriche, M., Uhlmann, M., Flores, O., García-Villalba, M.: Kinematics and dynamics of the auto-rotation of a model winged seed. Bioinspir. Biomim. **13**(3), 036011 (2018). doi:10.1088/1748-3190/aab144
3. Azuma, A., Yasuda, K.: Flight performance of rotary seeds. J. Theor. Biol. **138**(1), 23–53 (1989). doi:10.1016/S0022-5193(89)80176-6
4. van den Berg, C., Ellington, C.P.: The vortex wake of a 'hovering' model hawkmoth. Phil. Trans. R. Soc. Lond. B **352**(1351), 317–328 (1997). doi:10.1098/rstb.1997.0023

5. Birch, J.M., Dickinson, M.H.: Spanwise flow and the attachment of the leading-edge vortex on insect wings. Nature **412**(6848), 729–33 (2001). doi:10.1038/35089071
6. Birch, J.M., Dickson, W.B., Dickinson, M.H.: Force production and flow structure of the leading edge vortex on flapping wings at high and low Reynolds numbers. J. Exp. Biol. **207**(7), 1063–1072 (2004). doi:10.1242/jeb.00848
7. Chrust, M.: Etude numérique de la chute libre d'objets axisymétriques dans un fluide newtonien. Ph.D. thesis, Strasbourg (2012)
8. Ellington, C.P., Van Den Berg, C., Willmott, A.P., Thomas, A.: Leading-edge vortices in insect flight. Nature **384**(6610), 626 (1996). doi:10.1038/384626a0
9. Fregene, K., Bolden, C.L.: Dynamics and control of a biomimetic single-wing nano air vehicle. In: American Control Conference (ACC), 2010, pp. 51–56. IEEE (2010). doi:10.1109/ACC.2010.5531206
10. Garmann, D.J., Visbal, M.R.: Dynamics of revolving wings for various aspect ratios. J. Fluid Mech. **748**, 932–956 (2014). doi:10.1017/jfm.2014.212
11. Green, D.S.: The terminal velocity and dispersal of spinning samaras. Am. J. Bot. **67**(8), 1218–1224 (1980). doi:10.1002/j.1537-2197.1980.tb07754.x
12. Harbig, R.R., Sheridan, J., Thompson, M.C.: Reynolds number and aspect ratio effects on the leading-edge vortex for rotating insect wing planforms. J. Fluid Mech. **717**, 166–192 (2013). doi:10.1017/jfm.2012.565
13. Hunt, J.C.R., Wray, A.A., Moin, P.: Eddies, stream, and convergence zones in turbulent flows. Center For Turbulence Research **Report CTR-S88** (1988)
14. Jardin, T.: Coriolis effect and the attachment of the leading edge vortex. J. Fluid Mech. **820**, 312–340 (2017). doi:10.1017/jfm.2017.222
15. Jardin, T., David, L.: Spanwise gradients in flow speed help stabilize leading-edge vortices on revolving wings. Phys. Rev. E **90**(1), 013011 (2014). doi:10.1103/PhysRevE.90.013011
16. Lee, I., Choi, H.: Flight of a falling maple seed. Phys. Rev. Fluids **2**, 090511 (2017). doi:10.1103/PhysRevFluids.2.090511
17. Lee, S.J., Lee, E.J., Sohn, M.H.: Mechanism of autorotation flight of maple samaras (*Acer palmatum*). Exp. Fluids **55**(4), 1–9 (2014). doi:10.1007/s00348-014-1718-4
18. Lentink, D., Dickinson, M.H.: Rotational accelerations stabilize leading edge vortices on revolving fly wings. J. Exp. Biol. **212**(16), 2705–2719 (2009). doi:10.1242/jeb.022269
19. Lentink, D., Dickson, W.B., van Leeuwen, J.L., Dickinson, M.H.: Leading-edge vortices elevate lift of autorotating plant seeds. Science **324**(5933), 1438–1440 (2009). doi:10.1126/science.1174196
20. Limacher, E., Rival, D.E.: On the distribution of leading-edge vortex circulation in samara-like flight. J. Fluid Mech. **776**, 316–333 (2015). doi:10.1017/jfm.2015.279
21. Lugt, H.J.: Autorotation. Ann. Rev. Fluid Mech. **15**(1), 123–147 (1983). doi:10.1146/annurev.fl.15.010183.001011
22. Moriche, M.: A numerical study on the aerodynamic forces and the wake stability of flapping flight at low Reynolds number. Ph.D. thesis, Univ. Carlos III Madrid (2017)
23. Moriche, M., Flores, O., García-Villalba, M.: Three-dimensional instabilities in the wake of a flapping wing at low Reynolds number. Int. J. Heat Fluid Flow **62A**, 44–55 (2016). doi:10.1016/j.ijheatfluidflow.2016.06.015
24. Moriche, M., Flores, O., García-Villalba, M.: On the aerodynamic forces on heaving and pitching airfoils at low Reynolds number. J. Fluid Mech. **828**, 395–423 (2017). doi:10.1017/jfm.2017.508
25. Norberg, R.: Autorotation, self-stability, and structure of single-winged fruits and seeds (samaras) with comparative remarks on animal flight. Biol. Rev. **48**(4), 561–596 (1973). doi:10.1111/j.1469-185X.1973.tb01569.x
26. Obradovic, B., Ho, G., Barto, R., Fregene, K., Sharp, D.: A multi-scale simulation methodology for the samarai monocopter μUAV. In: AIAA Modeling and Simulation Technologies Conference, p. 5012 (2012). doi:10.2514/6.2012-5012
27. Pedersen, C.B., Żbikowski, R.: An indicial-Polhamus aerodynamic model of insect-like flapping wings in hover, *Flow Phenomena in Nature*, vol. 2, pp. 606–666. Liebe, R. (2006)
28. Poelma, C., Dickson, W.B., Dickinson, M.H.: Time-resolved reconstruction of the full velocity field around a dynamically-scaled flapping wing. Exp. Fluids **41**(2), 213–225 (2006). doi:10.1007/s00348-006-0172-3

29. Pounds, P., Singh, S.: Samara: Biologically inspired self-deploying sensor networks. IEEE Potentials **34**(2), 10–14 (2015). doi:10.1109/MPOT.2014.2359034
30. Salcedo, E., Treviño, C., Vargas, R.O., Martínez-Suástegui, L.: Stereoscopic particle image velocimetry measurements of the three-dimensional flow field of a descending autorotating mahogany seed (*Swietenia macrophylla*). J. Exp. Biol. **216**(11), 2017–2030 (2013). doi:10.1242/jeb.085407
31. Seter, D., Rosen, A.: Stability of the vertical autorotation of a single-winged samara. J. App. Mech. **59**(4), 1000–1008 (1992). doi:10.1115/1.2894014
32. Sun, M., Wu, J.: Large aerodynamic forces on a sweeping wing at low reynolds number. Acta Mechanica Sinica **20**(1), 24–31 (2004). doi:10.1007/BF02484241
33. Uhlmann, M.: An immersed boundary method with direct forcing for the simulation of particulate flows. J. Comput. Phys. **209**(2), 448–476 (2005). doi:10.1016/j.jcp.2005.03.017
34. Ulrich, E.R., Darryll, P., Humbert, J.S.: From falling to flying: the path to powered flight of a robotic samara nano air vehicle. Bioinspir. Biomim. **5**(4), 045009 (2010). doi:10.1088/1748-3182/5/4/045009
35. Varshney, K., Chang, S., Wang, Z.J.: The kinematics of falling maple seeds and the initial transition to a helical motion. Nonlinearity **25**(1), C1 (2012). doi:10.1088/0951-7715/25/1/C1
36. Yasuda, K., Azuma, A.: The autorotation boundary in the flight of samaras. J. Theor. Biol. **185**(3), 313–320 (1997). doi:10.1006/jtbi.1996.0299
37. Zhang, J., Liu, N., Lu, X.: Route to a chaotic state in fluid flow past an inclined flat plate. Phys. Rev. E **79**, 045306 (2009). doi:10.1103/PhysRevE.79.045306